Flow Separation Control over a Boeing Vertol VR-7 using NS-DBD Plasma Actuators

Ata Ghasemi Esfahani[1], Achal Singhal[1], Chris Clifford[1], Mo Samimy[2]

Gas Dynamics and Turbulence Laboratory, Aerospace Research Center
The Ohio State University, Columbus, Ohio 43235

The results of experiments designed to investigate excitation of flow over an airfoil with leading edge separation at a post-stall angle of attack with nanosecond pulse dielectric barrier discharge actuators are presented. The subject airfoil is designed with a small radius of curvature that potentially challenges the task of flow control as more centrifugal acceleration around leading is required to successfully reattach the flow. The Reynolds number based on the chord was fixed at $5 \cdot 10^5$, corresponding to a freestream flow of approximately 37 m/s. An angle of attack of 19° was used and a single plasma actuator was mounted near the leading edge of the airfoil. Fully separated flow on the suction side extended well beyond the airfoil with naturally shed vortices generated at a Strouhal number of 0.60. Excitation at very low (impulse excitation) to moderate (~1) Strouhal numbers at the leading edge generated organized coherent structures in the shear layer over the separated region with a shedding Strouhal number corresponding to that of the excitation, synchronizing the vortex shedding from leading and trailing edges. Excitation around the shedding Strouhal number promoted vortex merging while excitation at higher Strouhal numbers resulted in smaller, weaker structures that quickly developed and disintegrate over the airfoil. Excitation around the shedding Strouhal number significantly increased both the lift and drag, but high frequency excitation moved the separation point downstream and reduced both the lift and drag. The primary mechanism of control is the excitation of instabilities associated with the vortices shed from leading edge. The excitation generates coherent large-scale structures that entrain high-momentum fluid into the separation region to reduce the separation and/or accelerate the flow over the airfoil and to modify the lift and drag properties.

Nomenclature

C_D = drag coefficient
C_L = sectional lift coefficient
C_p = pressure coefficient
f = frequency
L = chord length, 203 mm
p = static pressure
p_∞ = freestream static pressure
q_∞ = freestream dynamic pressure
Re = Reynolds number based on chord, $u_\infty L/\nu$
St = Strouhal number, fL/u_∞
U = velocity vector, (u, v, w)

---

[1] Graduate Student, Department of Mechanical and Aerospace Engineering, AIAA Student Member
[2] The John B. Nordholt Professor of Mechanical and Aerospace engineering, Director of Aerospace Research Center, AIAA Fellow, Corresponding Author <samimy.1@osu.edu>

American Institute of Aeronautics and Astronautics

U^* = normalized velocity magnitude, $|U|/u_\infty$
u_∞ = freestream streamwise velocity
x = streamwise coordinate
y = vertical coordinate
α = angle of attack
λ_{ci} = swirling strength
λ_{ci}^* = non-dimensional swirling strength, $\lambda_{ci}c'/u_\infty$
ν = kinematic viscosity of air
ρ = density of air
ϕ = phase angle relative to plasma formation
ω = vorticity, $\nabla \times U$
ω^* = non-dimensional vorticity, $\nabla \times U/u_\infty$

I. Introduction

IMPROVING the performance of the rotorcrafts is of paramount importance if they are to meet the future challenges. Eliminating or at the very least alleviating flow separation over rotorcraft blades could potentially bring about significant performance improvements for this class of aircraft.

The relative airspeed approaching the retreating blade in rotorcraft is significantly lower than the airspeed approaching the advancing blade and this problem will become more pronounced as the forward speed is anticipated to increase and blade speed to decrease in the future rotorcraft. To compensate for the ensuing loss of lift due to a reduction in relative wind speed, the angle of attack of the retreating blade must increase so that the lift generated throughout the rotor disk is equally distributed. Flying at higher forward airspeeds necessitates a further increase in blade angle of attack and that would eventually lead to rotor stall. Commonly referred to as retreating blade stall, this phenomenon limits the highest speed that a rotorcraft can attain in forward flight[1]. Active flow control techniques have the potential to provide viable solutions for this problem and plasma-based actuators due to their wide bandwidth, high amplitude[2-4] and absence of moving parts are promising candidates for implementation of active flow on rotorcraft blades.

Dielectric barrier discharge actuators driven by AC waveforms have been shown to have control authority at relatively low Reynolds numbers but scaling their effect for successful implementation in high speed flows requires the use of thicker dielectrics and higher voltages[5-8]. Even when these changes are implemented, despite the fact that the body force produced by an actuator using a thick dielectric and driven by higher voltages might be as high as 20 times the body force induced by an actuator using a thin Kapton dielectric[9], there is a limit to the effectiveness of DBD actuators driven by AV waveform[7]. An alternative, first investigated by Roupassov et al.[10-12] is to supply the asymmetric single dielectric barrier discharge actuators with nanosecond high voltage DC pulses with pulse repetition rates that are varied from less than 100 Hz to several kHz. These actuators have demonstrated control authority at relatively higher flow speeds[12-19] as their control mechanism is not momentum-based, which is direct contrast to AC driven DBD actuators.

The results of the several studies conducted by Roupassov et al.[10,12], Little et al.[15], Che at al.[20], Popov at al.[21], Correale et al.[22], Starokovskii et al.[23] and Takashima et al.[24,25] point to the fact that nanosecond pulse driven DBD actuators mainly affect the flow through generating rapid, localized Joule heating that has a destabilizing effect and would trigger the instabilities in the flow that lead to the generation of coherent structures, which promote mixing in the flow[26-29]. A distinctive signature of the rapid localized heating generated by the mentioned actuators is the generation of fast moving compression waves that are originated near the discharge[23,24,26,28]. These waves have been reported to be formed by discharge filaments[23,28,30] but it is not clear whether they significantly contribute to the control authority of the NS-DBD actuators[26]. Reports by Correale at al.[22] and Dawson et al.[28] indicate that the strength of the compression waves strongly depends on discharge voltage.

This work aims to study the interaction of the nanosecond pulse driven DBD actuators installed over a VR-7 airfoil, which is typical of the rotorcraft blade. One particular aspect of the selected airfoil that seriously challenges successful implementation of any flow control technique is its small radius of curvature leading edge. According to Greenblatt and Wygnanski[31], larger momentum coefficients are required to achieve successful control over an airfoil with a smaller leading edge radius of curvature. Also notable in their study, which was focused on NACA 0012 and 0015 airfoils, was the conclusion that actuation at higher reduced frequencies was advantageous when implemented over NACA 0012 airfoil. Compared to a NACA 0012 airfoil, the model studied in this work designed with a leading edge that has a slightly smaller radius of curvature and this suggests that the previously reported unsteadiness in separation and reattachment near stall angle[31,32] might be observed.

Based on the preceding remarks, an important aspect of the present study that differentiates it from the works done on NS-DBD actuators hitherto is the implementation of these actuators on a thin, asymmetric airfoil with leading edge separation. Reports of the studies conducted by Little et al.[15,19], Correale et al.[22] and Rethmel et al.[17] on thick airfoils (NASA EET and NACA 0015 respectively) point the effectiveness of forcing at lower Strouhal numbers St ≈ O(1). In addition, in the small existing body of work on NS-DBD actuators the merits of forcing at higher Strouhal numbers, mentioned in the works of Amitay and Glezer[33] and Glezer et al.[34], are not explored and therefore there's no information on how the flow would respond when forced by a NS-DBD actuator at high frequencies. This works seeks to provide a better understanding in this particular area. Another area that has received particular attention in this work is the effect of actuation on shear layer development and wake vortex shedding. High-phase-resolution PIV measurements were carried out to elucidate the details of vortex merging and coherent structure development over the airfoil and in the wake region.

II. Experimental Facilities and Techniques

Experiments were performed in the recirculating wind tunnel located at the Gas Dynamics and Turbulence Laboratory, within the Aerospace Research Center at The Ohio State University[15]. The tunnel has an optically clear acrylic test section measuring 61×61 cm in cross-section and 122 cm in length. A Boeing Vertol VR-7 airfoil was used as it is a typical airfoil used in rotorcraft. The composite airfoil has a chord of $L = 20.3$ cm and is mounted in the center of the test section between two acrylic disks. The airfoil spans the entire span of the wind tunnel. The disks are able to rotate continuously, allowing for any angle of attack. The tunnel is capable of producing a continuous range of flow velocities from $3 - 95$ m/s. The corresponding Reynolds numbers based on chord length ($Re = u_\infty L/\nu$) are $0.04\cdot10^6 - 1.20\cdot10^6$. The angle of attack considered here was 19° at a Reynolds number based on chord of $0.50\cdot10^6$. The freestream turbulence intensity is on the order of 0.25% at this Reynolds number[19].

Freestream static pressure (p_∞) and stagnation pressure (p_o) are measured using piezometer rings consisting of four pressure taps. Located at either end of the converging section of the wind tunnel, these pressure taps are connected to Omega Engineering pressure transducers (models PXS655-25DI and PX655-5DI). Freestream temperature is measured using a thermocouple located downstream of the test section. This thermocouple is also used to obtain the ambient temperature prior to the startup of the tunnel. Ambient pressure data is recorded from METARs data reported by OSU Airport (KOSU). Free stream velocity can then be computed using Bernoulli's Equation:

$$u_\infty = \sqrt{2k\,\frac{p_o - p_\infty}{\rho}}$$

where $k = 1.05$, is the corrective factor and was empirically determined using a hot-wire anemometer[15].

Two coordinate systems are used throughout this paper. Both coordinate systems have their origin at the leading edge (LE), as shown in Fig. 1. The first system is a straight line along the chord line normalized by the chord length, denoted x/L, where positive coordinates indicate the aerodynamic suction side and negative coordinates indicate the aerodynamic pressure side. This system is in the airfoil reference frame and is used to indicate on-board instrumentation, actuators, and the flow separation line. The second system is a two-dimensional grid aligned with the test section and normalized by the chord, denoted x/L and y/L. This system is in the test section reference frame and is used to indicate other instrumentation, such as the microphone location (indicated by point A Fig. 1) and velocity data.
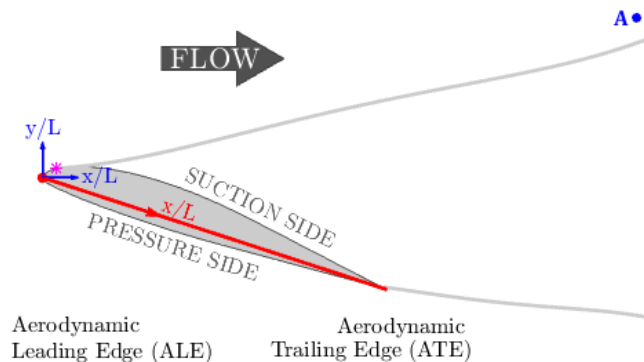

Fig. 1   Schematic of experimental arrangement showing the coordinate origin, actuator location, and location of the microphone (A).

American Institute of Aeronautics and Astronautics

A. Plasma Actuator and High Voltage Pulser

A single actuator was placed on the airfoil to evaluate the efficacy of excitation. The actuator is constructed of two 0.09 mm thick copper tape electrodes; the exposed high-voltage electrode is 6.35 mm (0.25 in) wide and the covered ground electrode is 12.70 mm (0.50 in) wide. The dielectric layer is composed of three layers of Kapton tape, each 0.09 mm thick with a dielectric strength of 10 kV. The total thickness of the entire actuator is 0.45 mm. The actuator was placed on the suction side of the airfoil with the electrode junction at $x/c = 0.04$.

The actuator is powered by a custom, in-house manufactured pulse generator. The pulse generator utilizes a magnetic compression circuit to create the input waveform for the actuator. A DC power supply supplying 450 VDC is used to power the pulse generator. The specifics of the pulse generator are discussed in previous work by Little[15] and Takashima[24,25]. Representative discharge characteristics were acquired for a ~570 millimeter long actuator driven at 100 Hz. Voltage and current traces are acquired using a LeCroy Wavejet oscilloscope (model 324A) simultaneously. A Tektronix high-voltage probe (model P6015A) is placed across the output terminals of the pulse generator and a Pearson current probe (model 2877) is placed on the ground output terminal of pulse generator (which is connected to the ground of the actuator). A total of 16 pulses were acquired and averaged. The voltage and current traces of this input waveform are shown in Fig. 2, along with the power and instantaneous energy traces.
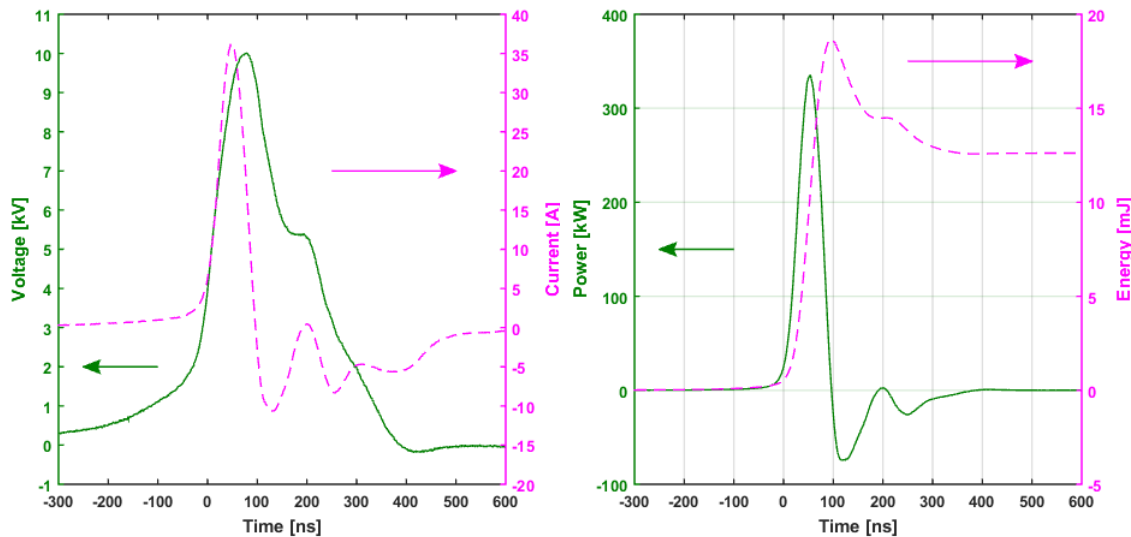

Fig. 2   Voltage-Current traces (left) and Power-Energy traces (right).

The peak voltage was 10 kV and the peak current was 36 A. The peak power consumption was 335 kW. However due to the narrow pulse width, the steady state energy consumption was 12.6 mJ per pulse. For the frequencies considered (less than 800 Hz), this corresponds to a time averaged power of 10 W. At the testing conditions, this corresponds to 3% of the freestream flow energy.

B. Static Pressure

Static pressure measurements on the airfoil surface were acquired using three Scanivalve digital pressure sensor arrays (DSA-3217). A total of 35 taps are located on the surface of the airfoil and the tap distribution is shown in Fig. 3. As indicated on the figure, 3 taps are covered by the plasma actuator. As such, data is from these three taps is ignored. The pressure coefficient, $C\_p = (p - p_\infty)/q_\infty$, was averaged over 105 samples acquired at 1 Hz near the centerline, where p is the static pressure, p_∞ is the freestream static pressure, and q_∞ is the freestream dynamic pressure. The sectional lift coefficient was calculated using the line integral $C_L = -\int_{-1}^{1} C_p \sin\theta \, ds$, where θ is the surface-normal angle and ds is the arc length. Similarly, the sectional pressure drag coefficient was calculated as $C_D = -\int_{-1}^{1} C_p \cos\theta \, ds$.
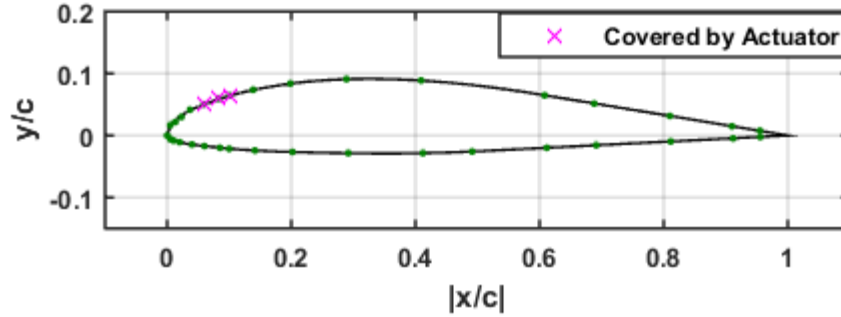
Fig. 3   Static pressure tap distribution for Boeing Vertol VR7 Airfoil.

C. Fluctuating Pressure Spectra

Pressure fluctuation measurements were collected and spectra were calculated to determine vortex shedding frequencies using a microphone. The microphone was found to be much more EMI-resistant than time-resolved pressure transducers or hot wire probes. Both baseline and forced pressure spectra were collected at a probe location of $x/c = 1.65$ and $y/c = 0.44$. This location is labeled as "A" in Fig. 1. A Brüel and Kjær model 4939 microphone and a Nexus 2690 signal conditioner (with a sensitivity of 3.16 mV/Pa) were used to acquire time-accurate pressure data. The data was collected in 60 blocks of 2^{14} samples each at a sampling rate of 10 kHz with a frequency resolution bandwidth of 0.61 Hz. The power spectral density was calculated for each block before the blocks were ensemble-averaged. The power spectral density was then converted into decibels using a reference pressure of 20 μPa. Strouhal numbers were calculated using the chord length of the airfoil, $St = fL/u_\infty$.

D. Particle Image Velocimetry

Particle image velocimetry (PIV) was the primary diagnostic technique. PIV is a quantitative technique that enables the mapping of the velocity and vorticity fields. PIV data was acquired for both the flow surrounding the suction side of the airfoil and behind the trailing edge. Maps of the normalized velocity magnitude, $U^* = U/u_\infty$, normalized vorticity, $\omega^* = \nabla^* \times U^*$, and turbulent kinetic energy, $TKE = \frac{1}{2}(u_{rms}^2 + v_{rms}^2)$, are shown to characterize the flow. In the plots, there is an arc, which from the acrylic disk the airfoil is fastened to, as shown in Fig. 4. It is not representative of any flow phenomenon.
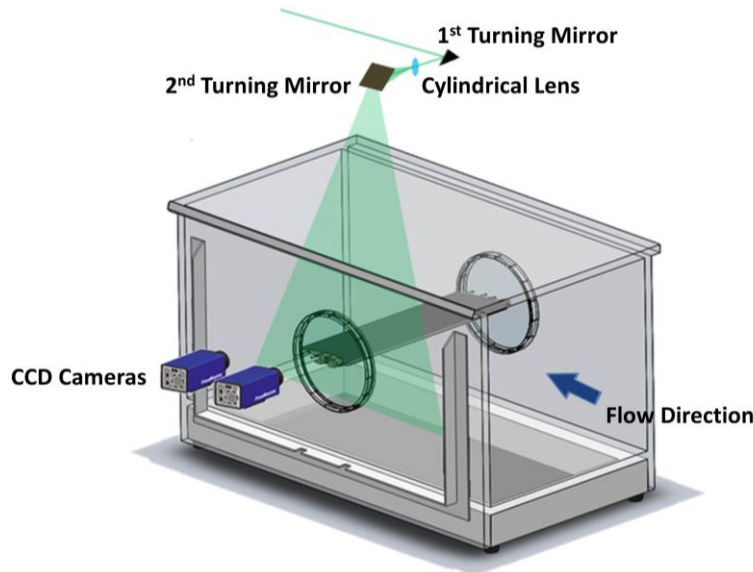

Fig. 4   Dual camera PIV experimental setup.

The seed particles were injected upstream of the test section. Extra virgin olive oil was atomized using a TSI 6-jet atomizer (model 9306A). The seed particles are illuminated using a Spectra Physics PIV-400 double-pulsed

American Institute of Aeronautics and Astronautics

Nd:YAG laser. The laser beam is formed into a sheet with the use of a 1 m focal length spherical lens and one 25 mm focal length cylindrical lens. Various turning optics were used to direct the laser sheet into the wind tunnel. The laser sheet has a thickness of ~2mm and is located at 60.4% (of the span of the airfoil) from the far end of the acrylic test section.

PIV was acquired using two LaVision 12-bit 2048x2048 pixels Imager Pro camera bodies, each with a Nikon Nikkor 35 mm f/1.2 lens. The cameras were positioned 253 mm center to center on a horizontal optical rail. The lenses of the cameras were located ~980 mm away from the laser sheet. The cameras acquired data simultaneously at an acquisition rate of 3.3 Hz. For excited cases, five sets of 100 image pairs were taken for a given case, where as in baseline data, a single set of 1000 images were taken.

For each image pair, a multi-pass cross correlation was used. The first window size used was 64x64 pixels with a 50% overlap, followed by two 32x32 pixels windows with a 75% overlap. The final pass was performed using a B-spline-6 reconstruction. The velocity fields were then post-processed to remove spurious vectors using a correlation peak ratio criterion, allowable vector range, and median filter based on nearest neighbor. The resulting velocity field was then smoothed using a 3x3 pixels Gaussian smoothing filter. Afterward, the images from each camera were stitched together and averaged.

Full scale error was computed using $\epsilon_{vel} = \epsilon_{cp}/(S\,dt)$, where ϵ_{vel} is the full scale error [m/s], ϵ_{cp} is the correlation peak estimation error [pixels], S is the scaling factor [pixels/m], and dt is the laser pulse separation [s]. The laser timing error was assumed to be negligible and ϵ_{cp} was taken to be 0.1 pixels[46]. As such, this corresponds to an error in instantaneous velocity of $0.74\ m/s$ (or 2% of the freestream velocity).

Three forms of PIV data was acquired – ensemble averaged, actuator phase locked, and pressure phase locked. Ensemble averaging of the instantaneous images provides a view of the time-averaged flow near the airfoil and in its wake.

The forcing mechanism was explored using phase-locked PIV. Instantaneous images were captured similar to baseline PIV, but were synchronized with specific phases throughout the forcing period and then phase-averaged. The phases considered here were $\phi = 0° - 330°$, with $30°$ increments. The delay between the trigger signal and plasma formation was accounted for so that plasma formation occurred at $\phi = 0°$. Swirling strength was used as the vortex identification technique, as detailed by Adrian *et al.*[45], and was non-dimensionalized to Strouhal number as described above.

An alternate phase locking method that synchronized with shedding of vortical structures, rather than plasma formation, was also employed. A Brüel and Kjær model 4939 microphone and a Nexus 2690 signal conditioner were used, as above, in conjunction with in-house software to provide a trigger signal based on vortex shedding events. The real-time software acquires pressure data, applies a first-order Butterworth band-pass filter about the shedding frequency, and outputs a square-wave trigger on a rising edge. A conditional averaging based on covariance was used in post-processing to filter out spurious trigger events. This method allows a phase-locked baseline to be acquired.

III. Results and Discussion

A. Static Pressure

Surface pressure data was obtained from 30 uncovered pressure taps (3 pressure taps were covered due to the presence of the actuator). The loss of the pressure taps near the leading edge does slightly affect the accuracy of the lift predicted. With the loss of these pressure taps, the coefficient of lift and coefficient of drag were 0.31 and 0.84 for a Strouhal number of 0 (no excitation). Given that the flow is fully separated, the loss of pressure taps is of little consequence in the baseline case. However in excited cases, the coefficient of lift would be underestimated.

The coefficient of pressure distribution is shown in Fig. 5 for a baseline case and several excitation Strouhal numbers. For excited case at a Strouhal number of 0.60, which is coincident with the natural shedding Strouhal number, the coefficient of pressure on the suction side has decreased significantly over the entire suction surface, which suggests that the flow has been accelerated when compared to the baseline case. However, the coefficient of pressure is nearly constant over the suction side and thus remains detached. This was confirmed by ensemble averaged PIV data acquisition, which will be presented later in the paper. At the higher excitation Strouhal number, the pressure gradient becomes more favorable $(\partial C_p/\partial(x/L) > 0)$. As such, the flow partially reattaches to the airfoil. Excitation at high Strouhal numbers, not only results in flow acceleration at the leading edge, but also contributes to pressure recovery in the aft portion of the airfoil, thus reducing the lift produced. Unfortunately, the loss of pressure taps in the leading edge means that the effect of partial reattachment of the flow in the leading edge

area cannot be registered by pressure sensors. Had the pressure taps been available and based on ensemble averaged PIV data, it is likely that a significant suction peak around the leading edge would have been observed.
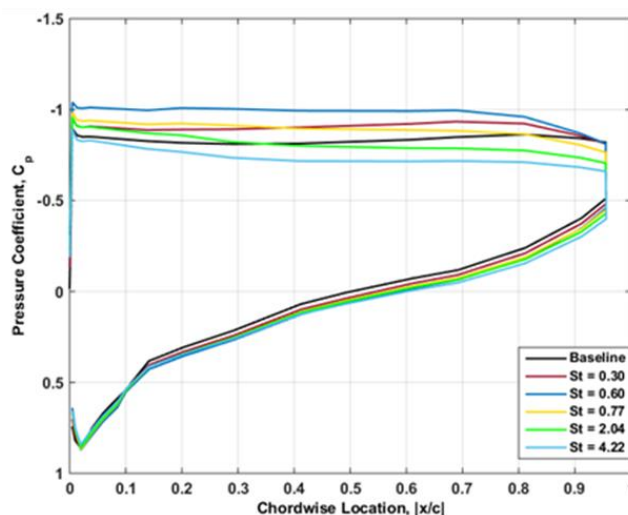

Fig. 5 **Coefficient of pressure distribution over Boeing Vertol VR7 airfoil at $\alpha = 19°$ and $Re = 500,000$.**

From the coefficient of pressure distributions, the coefficient of lift and drag can be computed via integration. Shown in Fig. 6 is the change in the coefficient of lift and drag from baseline values. It is observed that the coefficient of lift and drag follow a very similar trend – both attain a maximum when the actuators are excited at the natural Strouhal number. The mechanism through which the flow is influenced directly connects the changes in lift and drag together. The energy injected into the flow by the actuator excites natural instabilities that generate coherent structures. These structures remove energy from the freestream flow that results in an increase in drag. At the same time, the generated coherent vortices promote momentum exchange with the freestream flow, which accelerates the flow and amplifies the lift generated by the airfoil. As can be seen, the efficiency of this mechanism is directly dependent on the amplification of natural flow instabilities. As such, excitation at natural shedding Strouhal number ($St_e = 0.60$), which is the preferred mode Strouhal number, not only accelerates the flow, but also removes energy from it. Therefore the most considerable changes with respect to baseline are observed when the flow is actuated at this Strouhal number.

The maximum increase in the coefficient of lift is 22.2% and the maximum increase in the coefficient of drag is 17.5%. A local peak is also observed at the subharmonic of the natural Strouhal number. At higher excitation Strouhal numbers, both the coefficient of lift and drag decrease below the baseline values. This can be attributed to two factors. First, as the excitation Strouhal number is exceeds the preferred mode Strouhal number, the mechanism through which low-frequency forcing affects the flow becomes less efficient. Therefore, as suggested by Amitay and Glezer[33] and Glezer et al.[34] the forcing Strouhal number must be significantly increased to switch to the aerodynamic reshaping mechanism[35,36] which is potentially more effective than low-Strouhal number forcing[33]. Since the actuators used are capable of operating at much higher Strouhal numbers, this hypothesis will be explored in the next stage of the research.
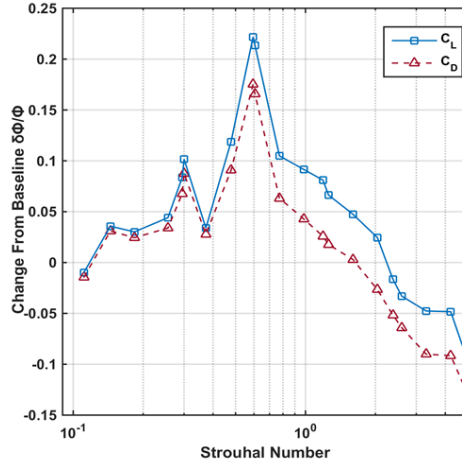
Fig. 6   Change in the coefficients of lift and drag.

B. Fluctuating Pressure Spectra

Fluctuating pressure data for various excitation Strouhal numbers using a microphone at a position of $x/L = 1.65$ and $y/L = 0.44$ is presented in Fig. 7. Each spectrum presented in the figure, has a label on the left, which indicates the excitation Strouhal number and is separated by 10 decibels from the curve above it for clarity. This figure does not provide absolute magnitude data and thus serves for the comparison of the shedding peaks. A well-defined, narrow-band peak at $St = 0.60$ and a harmonic with smaller amplitude at $St = 1.20$ can be readily seen in the baseline case. This suggests that there are strong and coherent vortices shed into the wake at $St = 0.60$. This is confirmed using pressure based phase-locked PIV data, which is discussed in the latter sections of the paper.

When the flow is excited at $St_e \leq 2$, a narrow peak at the excitation Strouhal number and at its harmonics are observed. The presence of the harmonics will be discussed further. In these cases, the harmonic closest to $St = 0.60$ has the largest amplitude as this is the preferred mode Strouhal number. For example, at $St_e = 0.26$, the most amplified Strouhal number is $St = 0.52$. This is because of the nature of the excitation – the frequency content of the high voltage pulse consists of both the excitation frequency, as well as its harmonics. Thus excitation at $St_e = 0.26$ also accomplishes excitation at $St_e = 0.52, 0.78, 1.04, etc$. At high excitation Strouhal numbers ($St_e > 2$), a well-defined narrow peak is not present.
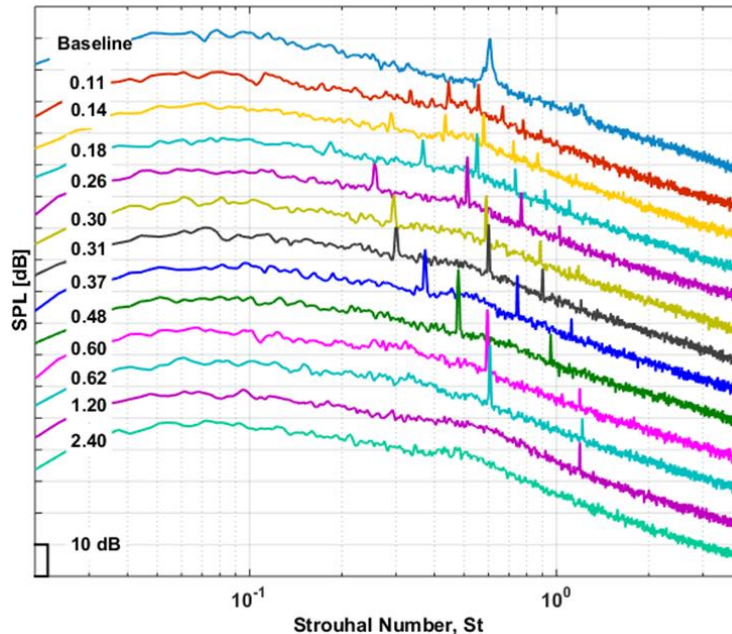

Fig. 7   Fluctuating pressure spectra acquired in the wake.

American Institute of Aeronautics and Astronautics

8

C. Ensemble Averaged Particle Image Velocimetry

PIV was acquired for the baseline and several excitation Strouhal numbers, however only a subset is shown in this section for $St_e = 0$ ($baseline$), $0.61, 2.04, and\ 4.21$. Ensemble-averaged normalized total velocity and vorticity are plotted in Fig. 8 and Fig. 9, respectively for these cases. In the excited cases, the formation of plasma causes velocity image corruption near the leading edge of the airfoil, and thus is not indicative of physical flow features. Also, the circular arc in the wake of the airfoil is caused by the mounting disk of the airfoil, and is not a flow feature.

For the excitation Strouhal numbers considered ($St_e < 5$), several studies in the past have identified signature characteristics of a flow forced at such Strouhal numbers[33–37]. Excitation at low Strouhal numbers primarily relies on the relatively narrowband receptivity of the separated shear layer and wake. Any forcing that would modify the global characteristics of the flow field via generating large-scale structures would promote mixing. According to Gelzer et al.[33,34] a Coanda-like deflection of the separated shear layer results in the convection of the shear layer vortices downstream in close proximity to airfoil surface and an increase in circulation around the airfoil, which a consequence of dominate shedding in the wake.

It must be noted that in such an approach to control, the time-scale of convection over the airfoil length is in the order of actuation period. This results in a potentially undesirable phenomenon in which periodic shedding of vorticity concentration into the wake bring about oscillations in the forces experienced by the airfoil[38]. This can be circumvented by forcing at higher frequencies as reported previously by several authors.

The normalized total velocity for the baseline case is shown in Fig. 8a. As is evident from the examination of this figure, at an angle of attack of $\alpha = 19°$ and a flow Reynolds number of 500,000 the flow is completely separated and a wake with a height commensurate with the projected frontal area of the airfoil forms. Upon careful examination of Fig. 8a, it seems that flow separates downstream of the leading edge. Surface oil flow visualization experiments will be conducted to verify this, but this could be due to an artifact of using a relatively wide angle lens so that a larger area of the flow may be examined.

Fig. 8 compares the normalized total velocity fields of the excited cases to the baseline flow field. The reduction in separation region area with an increase in forcing frequency is readily evident. It is interesting to note that excitation at higher excitation Strouhal numbers ($St_e > 2$), confines the low-speed recirculating flow region close to the airfoil surface and moves the separation point downstream. At $St_e = 4.21$, the separation point moves downstream – from $x/L = 0.1$ to $x/L = 0.24$. This can be attributed to shifting the development of large-scale structures upstream over the airfoil at relatively higher excitation Strouhal numbers, and better entrainment and mixing further upstream in the flow, which effectively reduces momentum deficit in the wake. Forcing at natural shedding Strouhal number brings about the most noticeable reduction in the cross-stream extent of the wake yet the shear layer leaves the surface right at the leading edge.

Another noteworthy observation is the change in the shape of the separating shear layer when flow is excited at $St_e = 2.06$ and $St_e = 4.21$. It appears that the shear layer is distorted at these particular frequencies, which might be due to the asynchronous shedding of the leading and trailing edge vortices.

Ensemble averaged plots of vorticity concentrations are shown in Fig. 9. For the baseline case, concentrations of clockwise vorticity are located above leading edge surface, where the shear layer separates, and downstream of the trailing edge. There are no vorticity concentrations immediately adjacent to airfoil surface. It should be noted that the well-defined clockwise and counter-clockwise vorticity layers extend far downstream of the airfoil trailing edge, which indicates vortices shed from the leading and trailing edge maintain their coherence and breakdown at a location further downstream of the trailing edge. This was further exemplified by the baseline phase-locked PIV data, which will be discussed in the latter sections.

As such, it is evident that excitation at $St_e = 0.61$ tilts the separated shear layer towards airfoil surface which is expected and is previously reported in a broadly similar configuration by Amitay and Glezer[33]. It is also interesting to note that excitation at $St_e = 2.06$ and $St_e = 4.21$ leads to shedding of smaller counter clockwise vorticity concentrations into the wake and weakening of clockwise vorticity concentrations downstream of the leading edge. This indicates that leading and trailing edge vortex formation behave independently. Excitation at excitation Strouhal numbers higher than the natural shedding Strouhal number ($St_e > 0.61$) leads to the formation of weak, incoherent structures that quickly breakdown. As such, the presence of these structures is not felt by the microphone, which is located in the wake. Another notable aspect is the persistence of diffused clockwise vorticity concentrations into the wake when the flow is excited at St = 2.06 and 4.21. Again, this is indicative of better mixing because of early breakdown of coherent structures.
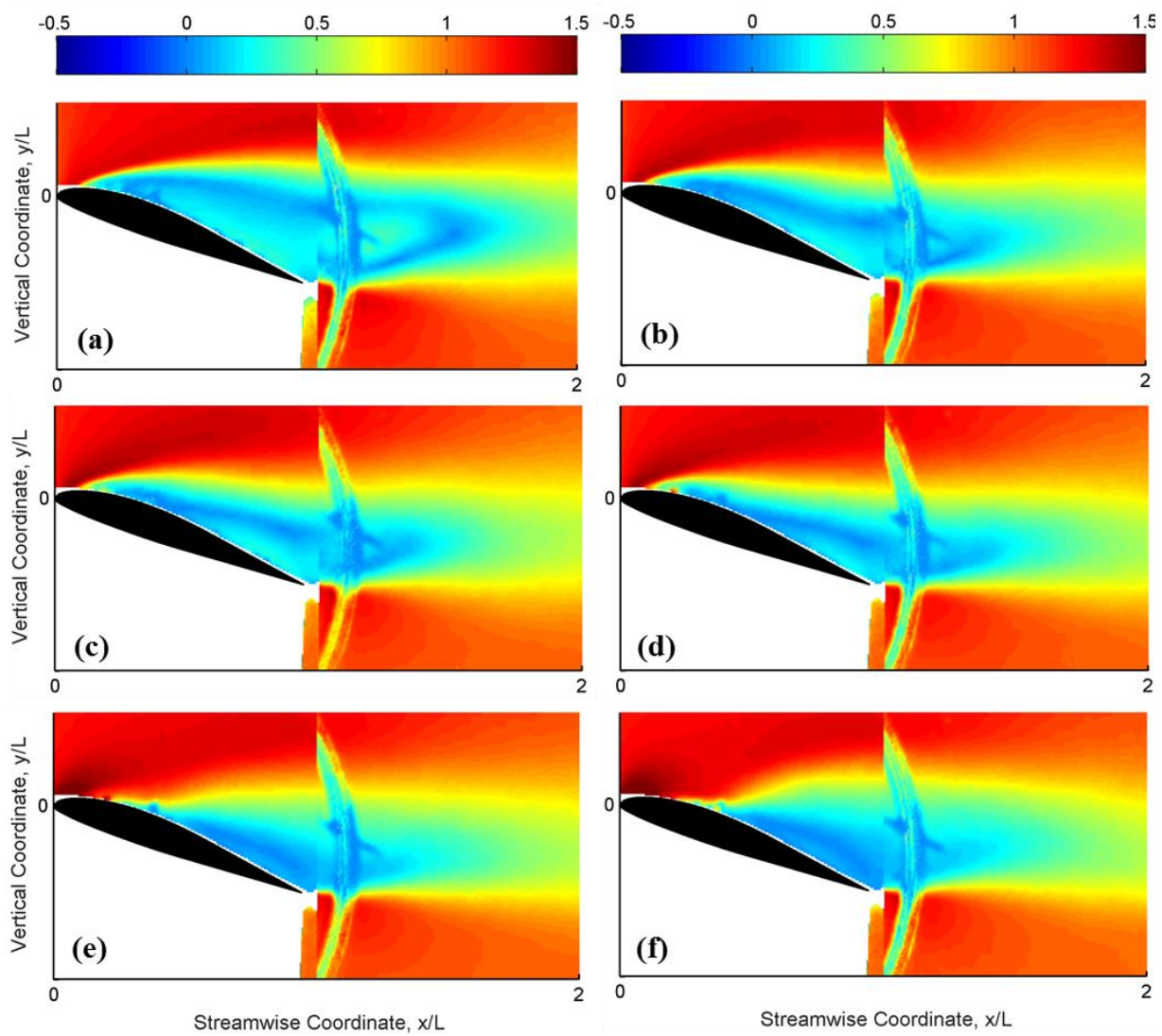
Fig. 8   Normalized Total Velocity, U^* for a) $St_e = 0$, b) $St_e = 0.61$, c) $St_e = 2.04$, d) $St_e = 4.21$.
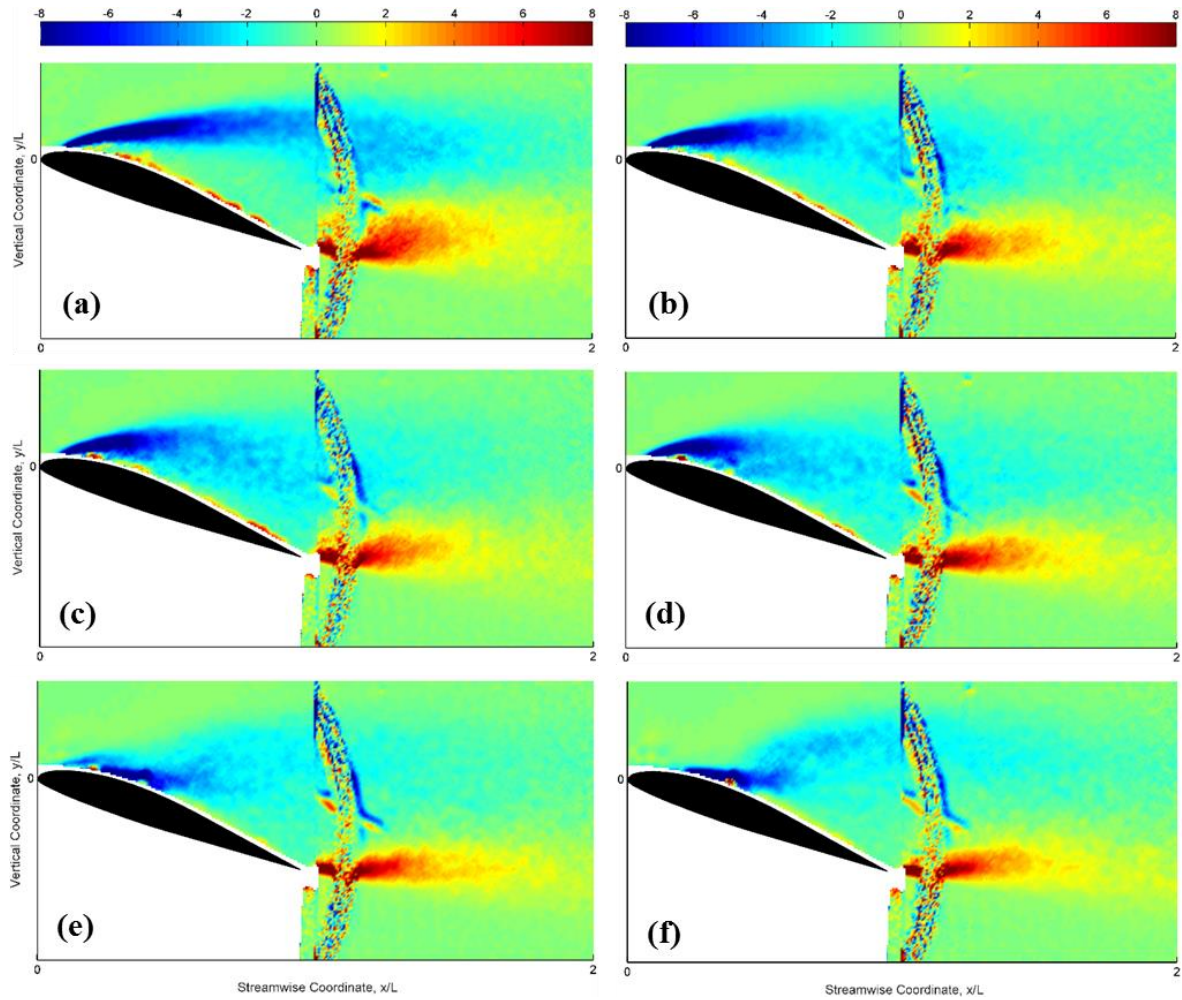
Fig. 9 Normalized Vorticity, ω^* for a) $St_e = 0$, b) $St_e = 0.61$, c) $St_e = 2.04$, d) $St_e = 4.21$.

D. Phase-locked Particle Image Velocimetry

In order to illustrate the development of coherent structures and merging under the effect of actuation by NS-DBD actuators, high-resolution phase-locked data was acquired for the baseline case and excitation at the shedding Strouhal number, $St_e = 0.61$ at 12 phases. For the baseline case, a microphone is placed in the wake (as done for the fluctuating pressure spectra) to be used as a reference for the phase-locking. For the excited case, the actuator signal is used for phase-locking. Fig. 10 shows the non-dimensionalized phase-locked swirling strength for the baseline case. As indicated in the figure, there is clear synchronized vortex shedding from the leading and trailing edges. There are structures formed at the leading edge, but these structures are not as coherent the trailing edge structures. Although not immediately clear, there is vortex merging seen at $\phi = 0°, 30°, and\ 60°$.

Fig. 11 shows the non-dimensionalized swirling strength for the excited case. This figure indicates a better-defined leading edge vortex. Particularly interesting is the merging process. The inception of the merging process can be seen at $\phi = 120°$. The core of the upstream vortex is located at $x/c = 0.6$ and begins to merge with the vortex located near the trailing edge as the trailing edge vortex begins to breakdown and disintegrate. At phase $\phi = 150°$, the first vortex is convected further downstream and begins to merge with the vortex near trailing edge. Consequently, a coherent structure with double the wavelength of the original vortices is generated at phase $\phi = 210°$ and is shed into the airfoil wake. It must be noted that in all phases, and at this excitation Strouhal number ($St_e = 0.61$), the vortices shed from LE and TE are synchronous with no phase lag. As noted before, this is not the case when flow is forced at higher excitation frequencies. By comparing the baseline and excited cases presented in Figures 11 and 12, it is evident that the vortices shed from trailing edge are noticeably weakened when the flow is forced.
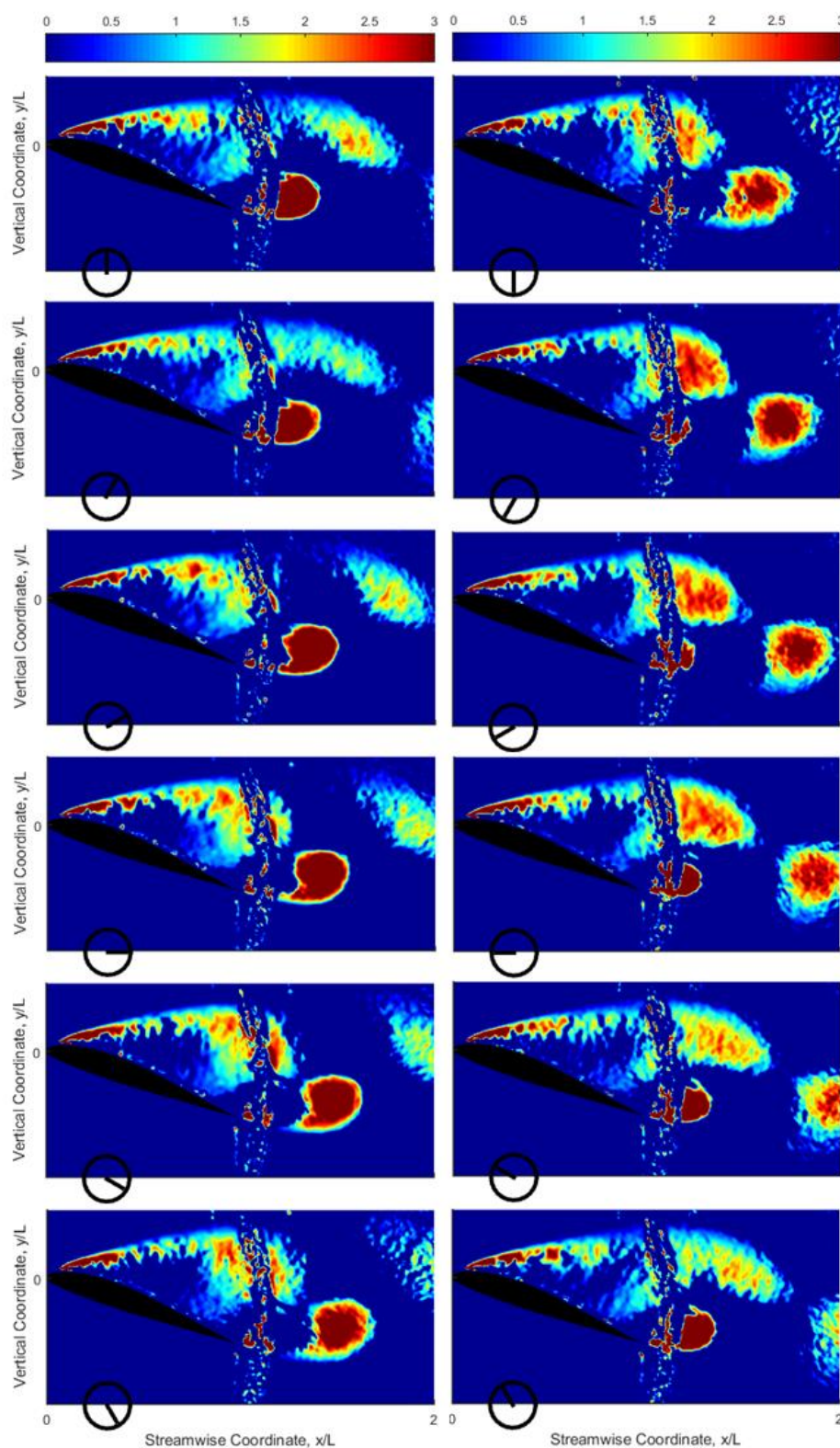
American Institute of Aeronautics and Astronautics

11

Fig. 10   Non-dimensionalized phase-averaged swirling strength, λ_{ci}^* for $St_e = 0$ (baseline) – phases ordered from top to bottom, then left to right.
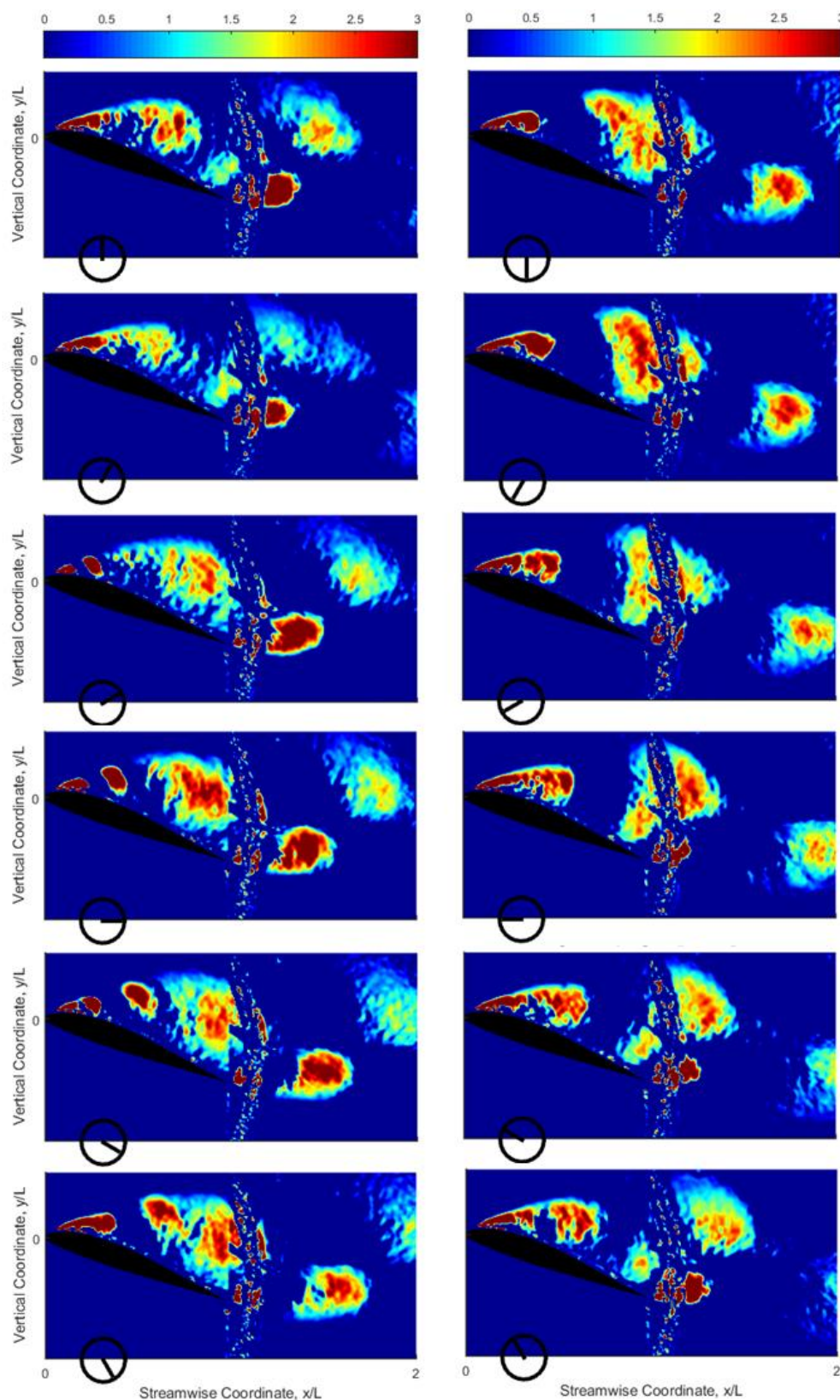
Fig. 11   Non-dimensionalized phase-locked swirling strength, λ_{ci}^* for $St_e = 0.61$ – phases ordered from top to bottom, then from left to right.

E. Discussion of Results

Leading edge excitation using a NS-DBD plasma actuator was explored in the present work. He et al.[39] investigated leading and trailing edge flow control using AC-DBD actuators in both a steady and unsteady manner on a NACA 0015 airfoil at $Re = 0.217 \cdot 10^6$ and $0.307 \cdot 10^6$. AC-DBD excitation imposes a body force on the near-wall fluid, thus functioning via momentum addition. This differs fundamentally from NS-DBD excitation, which generates thermal perturbations that manifest as pressure waves and excite natural flow instabilities[19]. Despite these differences, the unsteady excitation used by He *et al.* is still relevant. The leading edge unsteady excitation resulted in the production of coherent structures over the separated region[39], similar in nature to those of many others using plasma[7,19,40] and synthetic jets[41,42]. Similar structures are shown in Fig. 11 at $St_e = 0.61$. Despite the differences in their actuation nature, it is clear that NS-DBD plasma actuators are an effective flow control tool. Unlike Little et al.[15], who observed complete reattachment of the flow in a NACA 0015 airfoil, only partial reattachment was observed in this VR-7 airfoil. The difference is attributed to the significant difference in the nature of the airfoil, especially near the leading-edge.

At lower excitation Strouhal numbers, the actuators generate coherent spanwise structures that traverse the length of the airfoil. These vortices entrain high momentum fluid into the separated zone, increasing the lift produced. When the excitation Strouhal number increases, such that the structures development and disintegration move further upstream over the airfoil, the separation point moves downstream (Fig. 8). This results in the velocity increase near the wall to decrease the separation zone (Fig. 8) and is reflected in the static pressure data (Fig. 5).

Given that the NS-DBD excitation excites natural flow instabilities to generate coherent spanwise structures, the excitation Strouhal number determines the size and separation of the vortices. This is reflected in the ensemble averaged PIV data (Fig. 8 and Fig. 9). The flow responds to the excitation over a large range of Strouhal numbers, as shown in Fig. 6. From a controls perspective, this allows for an easier to implement scheme. Even at low excitation Strouhal numbers, actuation causes the creation of coherent structures that convect downstream.

It has been shown that NS-DBD operates based on thermal perturbations rather than momentum injection as in AC-DBD actuators[19]. These perturbations are amplified by natural flow instabilities. This has been demonstrated in other flows such as jets and cavities using a different plasma actuators called localized arc filament plasma actuators, LAFPAS[43,44]. The main flow instability in such flows is the free shear layer instability, the most amplified frequency of which scales with the initial momentum thickness. However, there is an imposed length scale in these flows (e.g. cord length or blockage height in the airfoil, which establishes the preferred mode frequency, which is the natural shedding frequency; nozzle exit diameter in jets and cavity length or depth in cavity flows). The two frequencies are at least an order of magnitude different. In NS-DBD or LAFPAs, the input signal is rectangular, rather than sinusoidal. Consequently, the actuation contains not only the forcing frequency, but also its harmonics (Fig. 7). Therefore, the actuations excite the shear layer instability, but multiple vortex mergings takes place to get from the shear layer frequency to the preferred mode frequency. This is supported by the excited phase locked PIV results shown in Fig. 11 that indicates vortex merging phenomena.

IV. Conclusions and Future Work

Flow control experiments were performed using a NS-DBD actuator on a Boeing VR7 airfoil installed in a recirculating wind tunnel such that the flow was fully separated. A 19° angle of attack at a Reynolds number of $0.50 \cdot 10^6$ was selected for detailed investigation. Fully separated flow on the suction side extended well beyond the airfoil with highly asymmetric velocity and vorticity fields and a shedding Strouhal number of 0.60.

NS-DBD plasma actuators generated organized coherent structures in the shear layer over the separated region, which convected into the wake region and moved the separation point downstream. Excitation around $St_e = 0.61$, the shedding Strouhal number, had the most significant effects: creating moderately sized structures that convect far downstream, increasing the lift and drag by 22.2% and 17.5%, respectively. Excitation at much higher Strouhal numbers resulted in the formation of smaller structures that attached the flow and moved the separation point downstream. As such, both the drag and lift were reduced. With excitation at low to moderate excitation Strouhal numbers, large-scale structures in the shear layer over the separated zone become more coherent and increase their entrainment abilities to bring high-momentum fluid into the separation region and affecting the lift and drag.

To better understand the effect of excitation on the nature of coherent structures generated over the airfoil, future work will include high-phase resolution phase-locked PIV data that will be acquired at low and high excitation Strouhal numbers. As of now, it's not clear whether aerodynamic reshaping via exciting the flow at high Strouhal numbers could be effectively implemented by NS-DBD actuators. Time-averaged PIV data will be acquired under such excitation conditions to investigate flow field modifications introduced. It is not immediately evident which effect generated by NS-DBD actuators, propagating shockwaves or thermal perturbations, play a more important

role in the control authority exerted by this class of actuators in various flow regimes. A comparison between vorticity plots with maps of density gradient obtained from Schlieren images would elucidate any possible connection between the thermal perturbations generated by the NS-DBD actuators and generation of vorticity in the flow. Any correlation between streamwise velocity fluctuations and strength of the generated shockwaves would illustrate the role of shockwaves in NS-DBD actuators' control effectiveness. Acquiring Schlieren data for forcing at various Strouhal numbers would be the next step towards better understanding the interaction between NS-DBD actuators and flow field.

Acknowledgements

References

[1] Leishman, J. G., *Principles of Helicopter Aerodynamics*, Cambridge University Press, 2006.

[2] Moreau, E., "Airflow control by non-thermal plasma actuators," *Journal of Physics D: Applied Physics*, vol. 40, 2007, p. 605.

[3] Samimy, M., Adamovich, I., Webb, B., Kastner, J., Hileman, J., Keshav, S., and Palm, P., "Development and characterization of plasma actuators for high-speed jet control," *Experiments in Fluids*, vol. 37, Aug. 2004, pp. 577–588.

[4] Benard, N., and Moreau, E., "Capabilities of the dielectric barrier discharge plasma actuator for multi-frequency excitations," *Journal of Physics D: Applied Physics*, vol. 43, 2010, p. 145201.

[5] Thomas, F. O., Corke, T. C., Iqbal, M., Kozlov, A., and Schatzman, D., "Optimization of Dielectric Barrier Discharge Plasma Actuators for Active Aerodynamic Flow Control," *AIAA Journal*, vol. 47, 2009, pp. 2169–2178.

[6] Patel, M. P., Ng, T. T., Vasudevan, S., Corke, T. C., Post, M., McLaughlin, T. E., and Suchomel, C. F., "Scaling Effects of an Aerodynamic Plasma Actuator," *Journal of Aircraft*, vol. 45, 2008, pp. 223–236.

[7] Wicks, M., Thomas, F., Schatzman, D., Bowles, P., Corke, T., Patel, M., and Cain, A., "A Parametric Investigation of Plasma Streamwise Vortex Generator Performance," *50th AIAA Aerospace Sciences Meeting including the New Horizons Forum and Aerospace Exposition*, American Institute of Aeronautics and Astronautics, .

[8] Wicks, M., Thomas, F. O., Corke, T. C., Patel, M., and Cain, A. B., "Mechanism of Vorticity Generation in Plasma Streamwise Vortex Generators," *AIAA Journal*, vol. 53, 2015, pp. 3404–3413.

[9] Kelley, C. L., Bowles, P. O., Cooney, J., He, C., Corke, T. C., Osborne, B. A., Silkey, J. S., and Zehnle, J., "Leading-Edge Separation Control Using Alternating-Current and Nanosecond-Pulse Plasma Actuators," *AIAA Journal*, vol. 52, 2014, pp. 1871–1884.

[10] Roupassov, D., Zavialov, I., and Starikovskii, A., "Boundary Layer Separation Plasma Control Using Low-Temperature Non-Equilibrium Plasma of Gas Discharge," *44th AIAA Aerospace Sciences Meeting and Exhibit*, American Institute of Aeronautics and Astronautics, .

[11] Roupassov, D., Starikovskii, A., Nikipelov, A., and Nudnova, M., "Boundary Layer Separation Control by Nanosecond Plasma Actuator," *44th AIAA/ASME/SAE/ASEE Joint Propulsion Conference & Exhibit*, American Institute of Aeronautics and Astronautics, .

[12] Roupassov, D. V., Nikipelov, A. A., Nudnova, M. M., and Starikovskii, A. Y., "Flow Separation Control by Plasma Actuator with Nanosecond Pulsed-Periodic Discharge," *AIAA Journal*, vol. 47, 2009, pp. 168–185.

[13] Marino, A., Catalano, P., Marongiu, C., Peschke, P., Hollenstein, C., and Donelli, R., "Effects of High Voltage Pulsed DBD on the Aerodynamic Performances in Subsonic and Transonic Conditions," *43rd Fluid Dynamics Conference*, American Institute of Aeronautics and Astronautics, .

[14] Peschke, P., Goekce, S., Leyland, P., Ott, P., and Hollenstein, C., "Experimental Investigation of Pulsed Dielectric Barrier Discharge Actuators in Sub- and Transonic Flow," *44th AIAA Plasmadynamics and Lasers Conference*, American Institute of Aeronautics and Astronautics, .

[15] Little, J., Takashima, K., Nishihara, M., Adamovich, I., and Samimy, M., "High Lift Airfoil Leading Edge Separation Control with Nanosecond Pulse DBD Plasma Actuators," *5th Flow Control Conference*, American Institute of Aeronautics and Astronautics, .

[16] Adamovich, I., Little, J., Nishihara, M., Takashima, K., and Samimy, M., "Nanosecond Pulse Surface Discharges for High-Speed Flow Control," *6th AIAA Flow Control Conference*, American Institute of Aeronautics and Astronautics, .

[17] Rethmel, C., Little, J., Takashima, K., Sinha, A., Adamovich, I., and Samimy, M., "Flow Separation Control over an Airfoil with Nanosecond Pulse Driven DBD Plasma Actuators," *49th AIAA Aerospace Sciences Meeting including the New Horizons Forum and Aerospace Exposition*, American Institute of Aeronautics and Astronautics, .

[18] Nishihara, M., Takashima, K., Rich, J. W., and Adamovich, I. V., "Mach 5 bow shock control by a nanosecond pulse surface dielectric barrier discharge," *Physics of Fluids (1994-present)*, vol. 23, Jun. 2011, p. 066101.

[19] Little, J., Takashima, K., Nishihara, M., Adamovich, I., and Samimy, M., "Separation Control with Nanosecond-Pulse-Driven Dielectric Barrier Discharge Plasma Actuators," *AIAA Journal*, vol. 50, 2012, pp. 350–365.

[20] Che, X., Shao, T., Nie, W., and Yan, P., "Numerical simulation on a nanosecond-pulse surface dielectric barrier discharge actuator in near space," *Journal of Physics D: Applied Physics*, vol. 45, Apr. 2012, p. 145201.

[21] Popov, I., Nikipelov, A., Pancheshnyi, S., Correale, G., Hulshoff, S., Veldhuis, L., Zaidi, S., and Starikovskiy, A., "Experimental Study and Numerical Simulation of Flow Separation Control with Pulsed Nanosecond Discharge Actuator," *51st AIAA Aerospace Sciences Meeting including the New Horizons Forum and Aerospace Exposition*, American Institute of Aeronautics and Astronautics, .

[22] Correale, G., Popov, I., Rakitin, A., Starikovskii, A., Hulshoff, S., and Veldhuis, L., "Flow Separation Control on Airfoil With Pulsed Nanosecond Discharge Actuator," *49th AIAA Aerospace Sciences Meeting including the New Horizons Forum and Aerospace Exposition*, American Institute of Aeronautics and Astronautics, .

[23] Starikovskii, A. Y., Nikipelov, A. A., Nudnova, M. M., and Roupassov, D. V., "SDBD plasma actuator with nanosecond pulse-periodic discharge," *Plasma Sources Science and Technology*, vol. 18, 2009, p. 034015.

[24] Takashima, K., Zuzeek, Y., Lempert, W., and Adamovich, I., "Characterization of Surface Dielectric Barrier Discharge Plasma Sustained by Repetitive Nanosecond Pulses," *41st Plasmadynamics and Lasers Conference*, American Institute of Aeronautics and Astronautics, .

[25] Takashima (Udagawa), K., Zuzeek, Y., Lempert, W. R., and Adamovich, I. V., "Characterization of a surface dielectric barrier discharge plasma sustained by repetitive nanosecond pulses," *Plasma Sources Science and Technology*, vol. 20, Oct. 2011, p. 055009.

[26] Leonov, S. B., Petrishchev, V., and Adamovich, I. V., "Dynamics of energy coupling and thermalization in barrier discharges over dielectric and weakly conducting surfaces on μ s to ms time scales," *Journal of Physics D: Applied Physics*, vol. 47, 2014, p. 465201.

[27] Akins, D. J., Singh, A., and Little, J. C., "Effects of Pulse Energy on Shear Layer Control using Surface Plasma Discharges," *45th AIAA Fluid Dynamics Conference*, American Institute of Aeronautics and Astronautics, .

[28] Dawson, R., and Little, J., "Characterization of nanosecond pulse driven dielectric barrier discharge plasma actuators for aerodynamic flow control," *Journal of Applied Physics*, vol. 113, Mar. 2013, p. 103302.

[29] Dawson, R. A., and Little, J., "Effects of pulse polarity on nanosecond pulse driven dielectric barrier discharge plasma actuators," *Journal of Applied Physics*, vol. 115, Jan. 2014, p. 043306.

[30] Peschke, P., Goekce, S., Hollenstein, C., Leyland, P., and Ott, P., "Interaction Between Nanosecond Pulse DBD Actuators and Transonic Flow," *42nd AIAA Plasmadynamics and Lasers Conference*, American Institute of Aeronautics and Astronautics, .

[31] Greenblatt, D., and Wygnanski, I., "Effect of Leading-Edge Curvature on Airfoil Separation Control," *Journal of Aircraft*, vol. 40, 2003, pp. 473–481.

[32] Sunneechurra, K., and Crowther, W. J., "Problems with Leading-Edge Flow Control Experiments," *Journal of Aircraft*, vol. 44, 2007, pp. 1052–1055.

[33] Amitay, M., and Glezer, A., "Role of Actuation Frequency in Controlled Flow Reattachment over a Stalled Airfoil," *AIAA Journal*, vol. 40, 2002, pp. 209–216.

[34] Glezer, A., Amitay, M., and Honohan, A. M., "Aspects of Low- and High-Frequency Actuation for Aerodynamic Flow Control," *AIAA Journal*, vol. 43, 2005, pp. 1501–1511.

[35] Amitay, M., Horvath, M., Michaux, M., and Glezer, A., "Virtual aerodynamic shape modification at low angles of attack using synthetic jet actuators," *15th AIAA Computational Fluid Dynamics Conference*, American Institute of Aeronautics and Astronautics, .

[36] Smith, D., Amitay, M., Kibens, V., Parekh, D., and Glezer, A., "Modification of lifting body aerodynamics using synthetic jet actuators," *36th AIAA Aerospace Sciences Meeting and Exhibit*, American Institute of Aeronautics and Astronautics, .

[37] Amitay, M., Smith, D. R., Kibens, V., Parekh, D. E., and Glezer, A., "Aerodynamic Flow Control over an Unconventional Airfoil Using Synthetic Jet Actuators," *AIAA Journal*, vol. 39, 2001, pp. 361–370.

[38] Seifert, A., Darabi, A., and Wyganski, I., "Delay of airfoil stall by periodic excitation," *Journal of Aircraft*, vol. 33, 1996, pp. 691–698.

[39] He, C., Corke, T. C., and Patel, M. P., "Plasma Flaps and Slats: An Application of Weakly Ionized Plasma Actuators," *Journal of Aircraft*, vol. 46, 2009, pp. 864–873.

[40] Clifford, C. J., and Samimy, M., "Flow Control on an Airfoil in Fully-Reversed Condition with Actuation on Both Leading and Trailing Edges," *53rd AIAA Aerospace Sciences Meeting*, American Institute of Aeronautics and Astronautics, .

[41] Weaver, D., McAlister, K. W., and Tso, J., *Suppression of Dynamic Stall by Steady and Pulsed Upper-Surface Blowing.*, 1996.

[42] Wu, J.-Z., Lu, X.-Y., Denny, A. G., Fan, M., and Wu, J.-M., "Post-stall flow control on an airfoil by local unsteady forcing," *Journal of Fluid Mechanics*, vol. 371, Sep. 1998, pp. 21–58.

[43] Yugulis, K., Hansford, S., Gregory, J. W., and Samimy, M., "Control of High Subsonic Cavity Flow Using Plasma Actuators," *AIAA Journal*, vol. 52, 2014, pp. 1542–1554.

[44] Samimy, M., Kim, J.-H., Kastner, J., Adamovich, I., and Utkin, Y., "Active control of high-speed and high-Reynolds-number jets using plasma actuators," *Journal of Fluid Mechanics*, vol. 578, May 2007, pp. 305–330.

[45] Adrian, R. J., Christensen, K. T., and Liu, Z.-C., "Analysis and Interpretation of Instantaneous Turbulent Velocity Fields," *Experiments in Fluids*, Vol. 29, 2000, pp. 275-290.

[46] Stanislas, M., Okamoto, K., Kähler, C. J., Westerweel, J., and Scarano, F., "Main Results of the third international PIV Challenge," *Experiments in Fluids*, Vol. 45, 2008, pp. 27-71.